

Quasi-periodic oscillations and reflection feature evolution in 4U 1630-47 observed with Insight-HXMT

JIASHI CHEN ¹ AND WEI WANG ¹

¹*Department of Astronomy, School of Physics and Technology, Wuhan University, Wuhan 430072, China*

ABSTRACT

The Galactic black hole (BH) X-ray binary 4U 1630-47 went into a new outburst in 2021 after ~ 600 days from its 2020 outburst. We perform a detailed analysis of quasi-periodic oscillations and spectral evolutions during its 2021 outburst based on *Insight*-HXMT observations. The main science aims to study the reflection features evolution of this accreting black hole using the observations of detecting quasi-periodic oscillations (QPOs) and quasi-regular modulations (QRMs). The QPOs frequencies evolve from $\sim 1.6 - 3.6$ Hz, and QRMs have low frequencies around 0.05 - 0.07 Hz. The reflection fraction varies during the outburst and has a positive correlation with the hardness ratio when QPOs are detected. The centroid frequency of QPOs is anti-correlated to the reflection fraction. This is consistent with the prediction of precessing inner flow model and provides evidence for a geometrical origin of QPOs. The centroid frequency of QRMs also shows an anti-correlation to the reflection fraction, but the hardness ratio shows no relation to the reflection fraction during the period. We suggest that QRMs may have a different origin from QPOs and be caused by instabilities in the corona.

Keywords: Black hole physics — X-rays: binaries — accretion, accretion disks

1. INTRODUCTION

Most black hole X-ray binaries are transient sources, characterized by alternating periods of dormancy marked by low flux or quiescent states, and outbursts featuring high flux or active states over their evolutionary trajectory. These transient systems primarily inhabit a quiescent phase with emissions remaining undetectable until the onset of outbursts. During outbursts, the X-ray emission experiences a significant surge, generally raising several orders of magnitude and displaying distinct spectral states (see [Remillard & McClintock 2006](#) for a review). During an outburst, black hole X-ray binaries typically cycle through several spectral states that can be traced using a hardness-intensity diagram (HID). In the HID, on the abscissa is the harness, which is defined as the ratio of the counts in a harder X-ray band to that in a softer X-ray band; on the ordinate is the total count rate over a broad energy band, which gives a proxy for luminosity and accretion rate (see, e.g., [Homan et al. 2001](#); [Belloni et al. 2005](#); [Homan et al. 2005](#)). The general evolution of an outburst in HID is a "q" shaped diagram that travels counterclockwise from the bottom right (see Figure 3 in [Remillard & McClintock 2006](#)). The right vertical branch corresponds to the Low/Hard State

(LHS) that characterized by large variability and a hard spectrum, which is observed at the start and the end of an outburst only. The left vertical branch corresponds to the High/Soft State (HSS), whose spectrum is soft, and the variability is low. The central part of the diagram identifies two intermediate states (IMS), the Hard Intermediate State (HIMS) and Soft Intermediate State (SIMS). During the IMS, the X-ray spectrum exhibits characteristics of both the LHS and the HSS. Although for different sources diagrams can look different in the HID, the sequence of states for the whole outburst generally follows as: LHS \rightarrow HIMS \rightarrow SIMS \rightarrow HSS \rightarrow SIMS \rightarrow HIMS \rightarrow LHS (see [Muñoz-Darias et al. 2011](#); [Belloni & Motta 2016](#) for a review).

Quasi-periodic oscillations (QPOs) can be observed in the light curves of X-ray binary systems during outbursts. QPOs are studied mainly in the Fourier domain and are found in the power spectrum, which is the squared modulus of the Fourier transform of the light curve ([van der Klis 1989](#)). In black hole X-ray binaries, QPOs with centroid frequency $\lesssim 30$ Hz are defined as low frequency (LF) QPOs, and QPOs with centroid frequency $\gtrsim 60$ Hz are defined as high frequency (HF) QPOs (see, e.g., [Belloni 2010](#)). HF QPOs are scarce and only a few candidates are observed, e.g., XTE J1550-564 ([Remillard et al. 2002](#)), XTE J1650-500 ([Homan et al. 2003](#)), GRO J1655-40 ([Remillard et al. 1999, 2002](#)), GRS 1915+105 ([Morgan et al. 1997](#); [Strohmayer 2001](#); [Belloni et al. 2006](#)). LF QPOs are frequently observed in BH X-ray binaries with

a high signal-to-noise, which allows detailed studies on the properties and origins of QPOs in the past few decades.

LF QPOs in BH X-ray binaries are generally classified into three types: A, B, and C (see [Wijnands et al. 1999](#); [Casella et al. 2005](#); [Motta et al. 2015](#); [Ingram & Motta 2019](#) for a review). Type-A QPOs are the least common LF QPOs in black hole X-ray binaries, e.g., GX 339-4 ([Motta et al. 2011](#)), XTE J1817-330 ([Sriram et al. 2012](#)), XTE J1859+226 ([Sriram et al. 2013](#)). Type-A QPOs are weak (few percent rms) and broad peaks in the power density spectra (PDS) with a centroid frequency of approximately 6-8 Hz in the power spectrum. Type-B QPOs have been detected in a large number of black hole X-ray binaries, e.g., GX 339-4 ([Motta et al. 2011](#)), XTE J1817-330 ([Sriram et al. 2012](#)), GRO J1655-40 ([Motta et al. 2012](#)), XTE J1859+226 ([Sriram et al. 2013](#)), 4U 1543-47 ([Russell et al. 2020](#)). Type-B QPOs with centroid frequencies typically at $\sim 5 - 6$ Hz, have a relatively high amplitude (up to $\sim 5\%$ rms) and are narrow ($Q \gtrsim 6$) peaks. Type-C QPOs are the most common type of QPOs in BH systems. Type-C QPOs are characterized by a high amplitude (up to 20% rms) and a narrow peak, with a wide frequency covering $\sim 0.1 - 30$ Hz. In the PDS of type-C QPOs, a broadband, flat-topped noise can also be observed, which may be caused by fluctuations of the accretion rate. The properties of LF QPOs are related to their spectral states. Type-C QPOs are usually observed in the hard state and hard intermediate state. Type-B and Type-A QPOs are generally found in the soft intermediate state. Transitions between different types of QPOs can sometimes be observed during state transitions. (see, e.g., [Sriram et al. 2013](#); [Zhang et al. 2021](#)).

In recent years, many theoretical models for the production of Type-C QPOs have been proposed. These models generally can be classified into two types: geometrical, the shape or size of something around the black holes varies quasi-periodically, such as the relativistic precession model (RPM) (see, e.g., [Stella & Vietri 1998](#); [Stella et al. 1999](#); [Schnittman et al. 2006](#)), the precessing inner flow model ([Ingram et al. 2009](#)), the corrugation modes model ([Kato & Fukue 1980](#); [Wagoner 1999](#); [Kato 2001](#)), the accretion ejection instability model ([Tagger & Pellat 1999](#)), the propagating oscillatory shock model ([Molteni et al. 1996](#); [Chakrabarti et al. 2008](#)); intrinsic, assuming the geometry of the system to be stable, with some resonant oscillations in properties of the disk, like density, pressure or accretion rate.

In recent years, some studies have provided evidence that Type-C QPOs may have a geometric origin. [Motta et al. \(2015\)](#) and [Heil et al. \(2015\)](#) statistically showed that Type-C QPOs are stronger in higher inclination binary systems. [van den Eijnden et al. \(2017\)](#) showed that small hard lags (i.e., hard photons lag soft photons) are seen when the Type-C QPO has a low frequency, and hard/soft lags are observed in low/high inclination sources when the Type-C QPO has a

high frequency. [Ingram et al. \(2016\)](#) showed that the centroid energy of the iron $K\alpha$ line varies with Type-C QPO phase. Therefore, reflection features (especially the iron line) contain information around the BH and its accretion disk, which may be able to provide valuable diagnostics for the physical origin of Type-C QPOs.

In addition to QPOs, oscillations with a period of ~ 10 -200 s have been observed in the light curve of some black hole candidates, e.g., 4U 1630-47 ([Trudolyubov et al. 2001](#)), GRS 1915+015 ([Morgan et al. 1997](#)), GRO J1655-40 ([Remillard et al. 1999](#)), IGR J17091-3624 ([Altamirano et al. 2011](#)), and H1743-322 ([Altamirano & Strohmayer 2012](#)). These variability patterns generally have a frequency of several tens of mHz and appear as a broad peak in the PDS. [Trudolyubov et al. \(2001\)](#) named these quasi-regular flares observed in 4U 1630-47 as quasi-regular modulations (QRMs). The most focused variability class of long-time quasi-regular flares or dips is the $\backslash\rho$ class (or “heartbeat” state). It’s characterized by regular X-ray flares typically lasting $\sim 40 - 200$ s (see, e.g., [Weng et al. 2018](#)). A possible origin of it is radiation-pressure-driven evaporation or ejections that happen at the inner region of the disk ([Neilsen et al. 2012](#)). The radiation pressure will be dominant at the inner region of the accretion disk, and when the mass accretion rate reaches a certain level, the limit-cycle behavior of the disk can lead to the modulation of flux due to the thermal viscous instability ([Lightman & Eardley 1974](#)). Tight correlations among the recurrence time, the inner radius of the disk, and the luminosity of the non-thermal emission have been found in the analysis of the “heartbeat” state ([Morgan et al. 1997](#)). And [Weng et al. \(2018\)](#) suggested that the “heartbeat” state in GRS 1915+105 may be caused by the variation of the corona size.

The spectra of BH X-ray binaries are generally composed of a black body component and a power-law component. The thermal black body component is generally considered to originate from a geometrically thin, optically thick accretion disk ([Shakura & Sunyaev 1973](#); [Novikov & Thorne 1973](#)). The turbulent stress will transport the angular momentum outward, and the disk material falls into the black hole releasing its gravitational potential energy. The inner disk will be heated and emit thermal emission. The accretion disk may evaporate and float into a large-scale height and play the role of the corona ([Eardley et al. 1975](#); [Ichimaru 1977](#)). Compton up-scattering of soft X-ray photons from the disk by the corona is commonly considered the origin of the power-law component ([Thorne & Price 1975](#); [Sunyaev & Truemper 1979](#)). The spectrum may also display a reflection component coming from the accretion disk reflecting the coronal emission. The reflected emission will be reprocessed by the disk’s upper atmosphere and re-emit with characteristic features such as an iron $K\alpha$ fluorescence line at $\sim 6.4 - 6.97$ keV, depending on the ionization of the iron ions, and a broad

Table 1. *Insight*-HXMT observations of 4U 1630-47 in the 2021 outburst with properties of detected QPOs and QRM (measured from the PDS in ME bands of 10-35 keV). The letter P indicates that the error of the parameter was pegged at the upper or lower boundary. All errors are calculated at 90 percent confidence level.

Num.	Observation ID	MJD	PDS	QPO/QRM			Broadband noise		$\chi^2/\text{d.o.f}$
				Centroid	Fractional	Q factor	Centroid	Fractional	
				Frequency (Hz)	rms (%)		Frequency (Hz)	rms (%)	
1	P040426300101	59475.647	QPO	$1.66^{+0.05}_{-0.05}$	$17.8^{+2.8}_{-3.8}$	$4.9^{+0.8}_{-1.6}$	$0.0^{+2.1}_{-P}$	$12.2^{+5.4}_{-8.4}$	140/117
2	P040426300201	59476.488	QPO	$2.43^{+0.03}_{-0.03}$	$15.3^{+1.3}_{-1.1}$	$8.2^{+0.2}_{-0.2}$	$0.0^{+0.2}_{-P}$	$17.5^{+1.7}_{-1.5}$	146/117
3	P040426300301	59477.647	QPO	$2.91^{+0.08}_{-0.07}$	$13.0^{+2.8}_{-1.8}$	$11.1^{+0.4}_{-1.0}$	$0.0^{+0.3}_{-P}$	$21.4^{+2.7}_{-2.5}$	133/117
4	P040426300401	59478.906	QPO	$3.54^{+0.08}_{-0.07}$	$15.1^{+2.1}_{-1.1}$	$6.3^{+0.4}_{-0.3}$	$0.0^{+0.1}_{-P}$	$24.4^{+1.2}_{-1.3}$	131/117
5	P040426300501	59479.647	None	None	None	None	$0.0^{+0.1}_{-P}$	$25.4^{+1.0}_{-1.1}$	165/117
6	P040426300601	59480.641	None	None	None	None	$0.0^{+0.1}_{-P}$	$23.9^{+1.1}_{-1.2}$	148/117
7	P040426300701	59481.667	QPO	$2.39^{+0.07}_{-0.08}$	$14.5^{+3.3}_{-4.7}$	$7.0^{+0.7}_{-0.8}$	$0.0^{+1.8}_{-P}$	$19.4^{+0.5}_{-0.7}$	141/117
8	P040426300801	59482.626	QPO	$3.27^{+0.11}_{-0.14}$	$16.4^{+2.5}_{-2.3}$	$3.9^{+0.6}_{-0.4}$	$0.0^{+0.2}_{-P}$	$23.0^{+0.2}_{-0.2}$	128/117
9	P040426300901	59483.785	QRM	$0.066^{+0.005}_{-0.003}$	$12.3^{+1.2}_{-1.0}$	$2.2^{+0.5}_{-0.3}$	$0.0^{+0.3}_{-P}$	$12.9^{+0.9}_{-1.1}$	288/218
10	P040426300902	59483.888	QRM	$0.066^{+0.002}_{-0.002}$	$14.0^{+0.8}_{-0.8}$	$3.5^{+0.2}_{-0.2}$	$0.0^{+0.1}_{-P}$	$11.3^{+0.8}_{-0.8}$	264/218
11	P040426300903	59484.022	QRM	$0.063^{+0.009}_{-0.004}$	$10.5^{+1.0}_{-0.8}$	$1.5^{+0.8}_{-0.4}$	$0.0^{+0.7}_{-P}$	$13.5^{+0.9}_{-1.7}$	240/218
12	P040426301001	59484.932	QRM	$0.054^{+0.003}_{-0.003}$	$14.0^{+0.9}_{-0.8}$	$1.7^{+0.2}_{-0.2}$	$0.0^{+0.3}_{-P}$	$12.8^{+0.9}_{-0.8}$	239/218
13	P040426301002	59485.050	QRM	$0.052^{+0.003}_{-0.001}$	$15.8^{+1.4}_{-1.6}$	$1.9^{+0.3}_{-0.1}$	$0.0^{+0.2}_{-P}$	$9.5^{+1.0}_{-1.2}$	249/218
14	P040426301003	59485.240	QRM	$0.056^{+0.002}_{-0.004}$	$10.9^{+1.1}_{-1.2}$	$3.5^{+0.7}_{-0.3}$	$0.0^{+0.2}_{-P}$	$8.4^{+0.5}_{-1.1}$	224/218
15	P040426301004	59485.373	None	None	None	None	$0.0^{+0.3}_{-P}$	$4.1^{+1.4}_{-1.4}$	125/117
16	P040426301005	59485.506	None	None	None	None	$0.0^{+0.1}_{-P}$	$2.1^{+2.2}_{-0.7}$	138/117

bump peaking at $\sim 20 - 30$ keV which is named as the Compton hump (Lightman & Rybicki 1980; García & Kallman 2010). The reflection features near the BH will be distorted by the relativistic motion of disk material and the gravity of the BH. As a result, the iron line profile appears asymmetrically broadened in the spectrum (Fabian et al. 1989; Dauser et al. 2010).

Black hole X-ray binary 4U 1630-47 is a transient source showing recurrent outbursts. It was first observed by Vela-5B during the 1969 outburst (Priedhorsky 1986). Since then, 4U 1630-47 goes into outbursts frequently and with a typical period of 600-700 days (Jones et al. 1976; Priedhorsky 1986; Parmar et al. 1995), and it is a part of the group of X-ray transients known as X-ray novae (Syunyaev et al. 1994; Tanaka & Shibazaki 1996). X-ray novae are assumed to be recurrent, with a typical outburst recurrence time of about 10-50 years. Therefore, only a single event is recorded in some sources (e.g., Chen et al. 1997; Grindlay et al. 2014). The source

4U 1630-47 lies in the direction toward the Galactic center and is heavily absorbed in the soft X-ray band, which implies a large distance to the source. Due to the large extinction amount of optical (>20 mag) and reddening effect, no optical counterpart has been identified and no dynamical mass measurement has been made at present (Seifina et al. 2014). Seifina et al. (2014) studied the correlation between the mass accretion rate and the photon index of spectra (observations that LF QPOs are observed), estimated 4U 1630-47 has a mass $\sim 10M_{\odot}$ and an inclination angle $i \leq 70^{\circ}$. Kalemci & Maccarone (2018) studied the dust-scattering halo created by 4U 1630-47 and estimated the distance to the source to be about 4.7-11.5 kpc. King et al. (2014) estimated an extremely high spin $a = 0.985^{+0.005}_{-0.014}$ and an inclination angle $i = 64^{+2}_{-3}$ deg by fitting the NuSTAR spectra. Liu et al. (2022) obtained a moderately high spin $a = 0.817 \pm 0.014$ from fitting the reflection spectra observed by *Insight*-HXMT during the 2020 outburst.

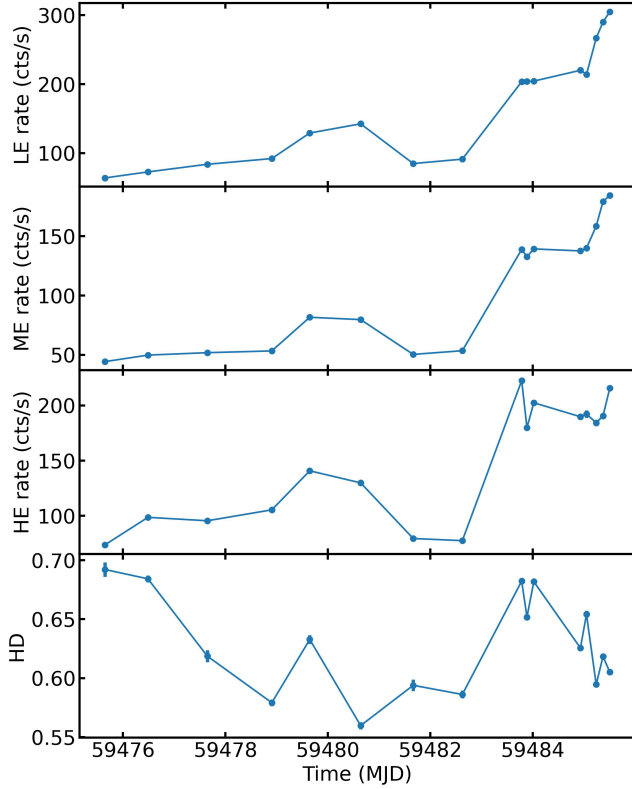


Figure 1. *Insight*-HXMT LE (2-10 keV), ME (10-35 keV), and HE (27-100 keV) light curves of the source, together with the variation of the hardness ratio defined as the ratio of the count rates between the ME 10-35 keV and LE 2-10 keV bands. The background rates are generally lower than the count rates of the source in corresponding energy bands.

In this work, we studied the quasi-periodic oscillations and spectral evolutions of the 4U 1630-47 based on *Insight*-HXMT observations of its 2021 outburst. In Section 2, we introduce the observations and data reduction process. The timing analysis on QPOs and QRM and spectral results are shown in Section 3. We briefly discuss our results and implications in Section 4. A concise conclusion of the work is given in section 5.

2. OBSERVATIONS AND DATA REDUCTION

The Hard X-ray Modulation Telescope *Insight*-HXMT is China’s first X-ray astronomy satellite, launched on 2017 June 15 (Zhang et al. 2020). It is a large X-ray astronomical satellite with a broad energy band of 1-250 keV. To fulfill the requirements of the broadband spectra and fast variability observations, three payloads are configured onboard *Insight*-HXMT: High Energy X-ray telescope (HE) for 20-250 keV band (Liu et al. 2020), Medium Energy X-ray telescope (ME) for 5-30 keV band (Cao et al. 2020), and Low Energy X-ray telescope (LE) 1-15 keV band (Chen et al. 2020). Light curves and spectra were extracted using *Insight*-HXMT Data

Analysis Software (HXMTDAS) v2.05 following the standard procedure (also see processing details described in Wang et al. 2021; Chen et al. 2021). In the data screening procedure, we use tasks *he/me/lepical* to remove spike events generated by electronic systems and *he/me/legtigen* to select good time interval (GTI) under the following conditions: the pointing offset angle $< 0.04^\circ$; the pointing direction above earth $> 10^\circ$; the geomagnetic cut-off rigidity > 8 GeV and no South Atlantic Anomaly (SAA) passage occurred within the previous 300 seconds. Background estimation was performed using *he/me/lebkmap*, and further refined using *lcmath* to eliminate estimated background noise. The dead-time effect is corrected using the nonparalyzable model proposed in Zhang et al. (1995).

Insight-HXMT started high-cadence monitoring of 4U 1630-47 from 2021 September 18 to 28 and stopped after 2021 September 28 owing to the small solar aspect angle ($< 70^\circ$, Yang et al. 2022). The observations we studied in this work are listed in Table 1, they are observed by *Insight*-HXMT. These observations are in the hard state or hard intermediate state and display reflection features in the spectra. Therefore, we fit the spectra with the reflection model and study the reflection features. In this work, we analyzed the spectra using 2-8 keV for LE, 8-28 keV for ME, and 28-100 keV for HE.

We employ *powspec* from HEASOFT to calculate the PDS for each observation to obtain the properties of QPOs and QRMs. We use a time interval of 128 s and a corresponding time resolution of 1/128 s for the QPO signals and a time interval of 256 s and a corresponding time resolution of 1/64 s for the QRM signals. The PDS are rebinned in frequency space using a geometric factor of 1.05. The PDSs were normalized to units of $\text{rms}^2 \text{Hz}^{-1}$ and subtracted Poisson noise following the methods described in Belloni & Hasinger (1990) and Miyamoto et al. (1991). We utilized multiple Lorentz functions to fit the profiles of the broadband noises and QPOs/QRMs in the PDS. This approach allows us to extract the fundamental parameters of the QPOs/QRMs. The fractional rms of the QPOs/QRMs is calculated:

$$\text{rms}_{\text{QPO}} = \sqrt{R} \times \frac{S+B}{S}, \quad (1)$$

where S is the source count rate, R is the normalization of the Lorentzian component, and B is the background count rate (see, e.g., Bu et al. 2015; Zhu & Wang 2024). And obtain the quality factor $Q = \nu/\Delta\nu$ (where ν represents the frequency of the QPO and $\Delta\nu$ represents the full width at half maximum, FWHM).

3. ANALYSIS AND RESULTS

Figure 1 presents the background-subtracted light curves from *Insight*-HXMT in three energy bands (LE, ME, and HE) and the hardness ratios (count ratio of ME to LE). We create

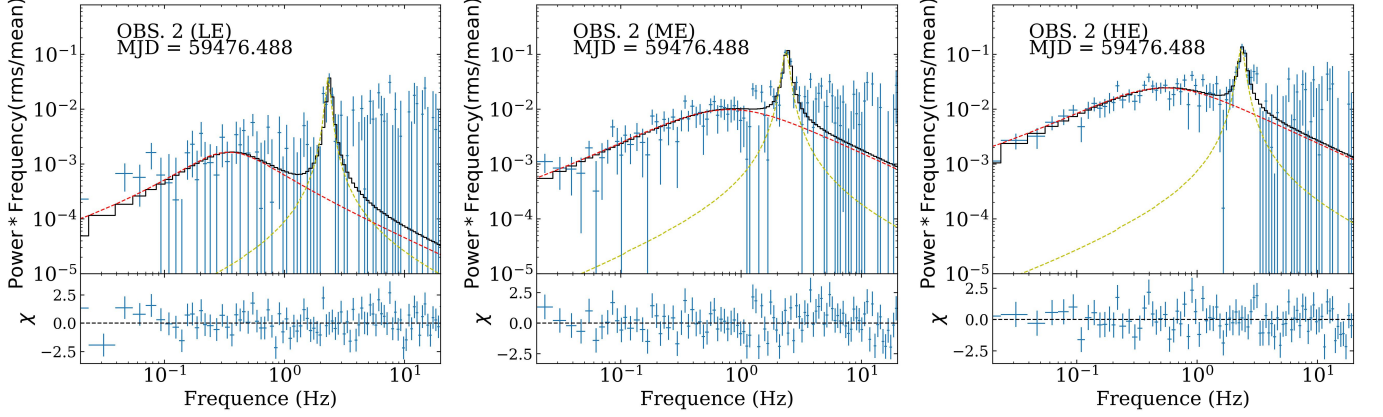


Figure 2. The representative fitting results of the QPO signals observed in 4U 1630-47 with Insight-HXMT. **Left:** PDS of OBS. 2 calculated from the LE band (2 - 10 keV), the QPO signal is weaker with the rms $\sim 7\%$. **Middle:** PDS of OBS. 2 calculated from the ME band (10 - 35 keV) shows the QPO feature around 2.5 Hz. **Right:** PDS of OBS. 2 calculated from the HE band (27 - 100 keV), the properties of QPO are similar to the ME band.

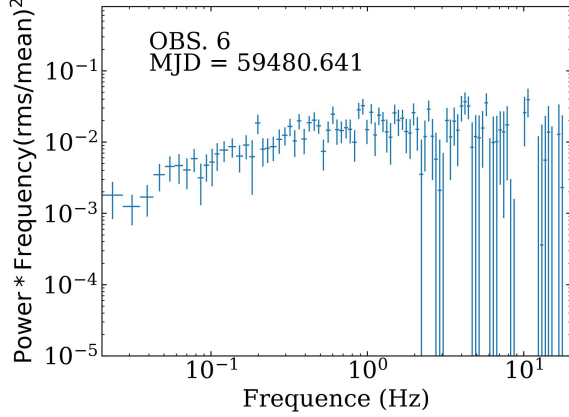


Figure 3. The representative PDS (ME band, 10 - 35 keV) of no evident QPO signals.

an averaged power spectrum for each observation to study the fast X-ray variability. Examples of the PDS are shown in Figures 2, 3, and 4, accompanied by respective model fitting results. The evolution of both frequency and fractional rms of QPOs and QRM is shown in Figure 5. The QPOs in HE and LE bands of OBS. 2 have similar frequencies to that in the ME band, but the signal is weaker (fractional rms $\sim 7\%$) in the LE band. Apart from Obs. 2, the PDSs of other observations also show very weak or no QPO signal in LE and HE bands. Therefore, we use ME band light curves to calculate the PDS and QPO properties in the following. The fitting results of all QPOs and QRMs are listed in Table 1. From MJD 59475.6-59482.6 (OBS. 1-4, 7-8), the PDS features a relatively narrow QPO peak centered at 1.6-3.6 Hz, accompanied by a broadband noise. The frequency of the QPOs is anti-correlated with the spectral hardness ratio. The Q factors are in the range of $\sim 4 - 11$, with fractional rms amplitudes of $\sim 12\% - 17\%$. Based on these characteristics, these QPOs can be identified as Type-C QPOs (see, e.g., [Wijnands et al. 1999](#);

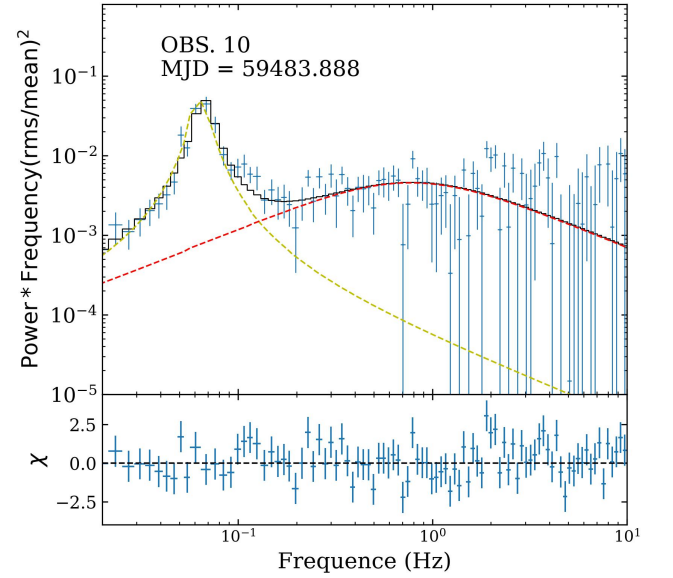


Figure 4. The representative fitting result of the QRM signals observed in 4U 1630-47 with Insight-HXMT. The figure is the PDS of OBS. 10 calculated from the ME band, and shows the QRM feature around 0.06 Hz.

[Casella et al. 2005](#)). From MJD 59483.8-59485.2 (OBS. 9-14), the PDS features a relatively broad peak near 60 mHz (named QRM) along with a broadband noise component. The QPOs are observed when the flux is low and the QRMs are observed in a certain range of flux (e.g., ME 10-35 keV count rates $\sim 120 - 150 \text{ counts s}^{-1}$).

During the Insight-HXMT observations, the source was located in the hard and intermediate states (see Figure 2 in [Yang et al. 2022](#)), which would be suitable to study non-thermal spectral properties, e.g., reflection features. We used spectral analysis software Xspec v12.14.0 to study the spectra ([Arnaud 1996](#)). Firstly, we fit the spectra with a phenomeno-

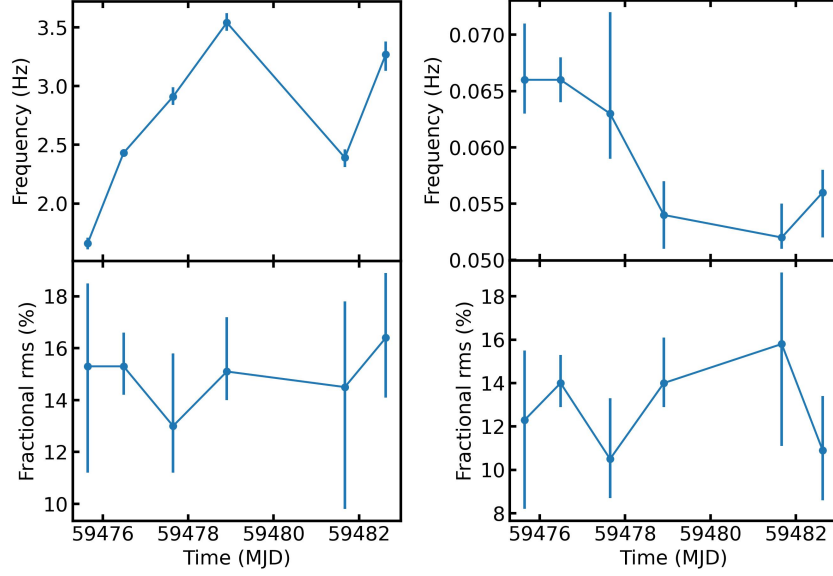


Figure 5. The evolution of the frequency and fractional rms for both QPOs and QRMs. **Left:** the evolution of QPOs. **Right:** the evolution of QRMs.

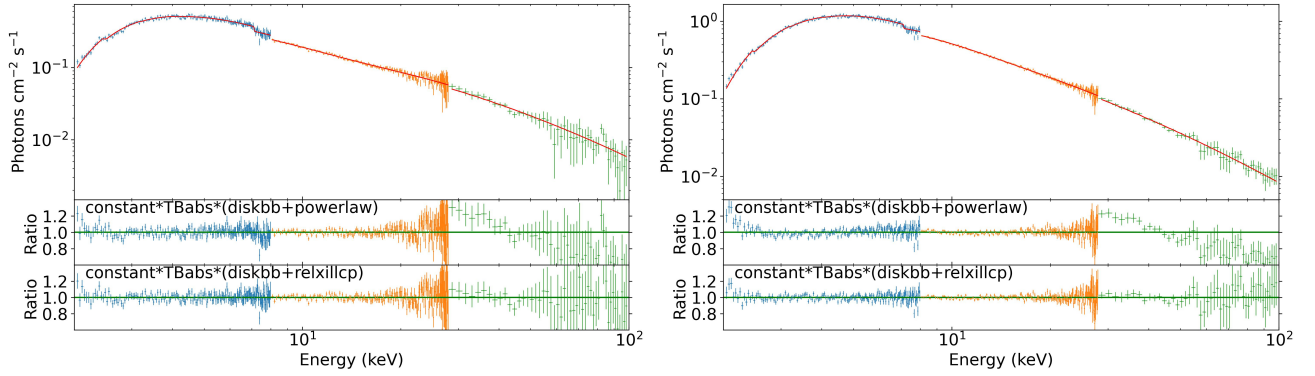


Figure 6. The best-fitting results and the corresponding data-to-model ratios of the three spectra using LE, ME, and HE detectors. The spectra are fitted with model `constant*tbabs(diskbb+relxillcp)`. **Top:** Observation Num. 4, when QPO is detected. **Bottom:** Observation Num. 10, when QRM is detected.

logical model `constant*tbabs(diskbb+powerlaw)`. Figure 6 shows two examples of spectral fitting results, OBS. 4 (QPO) and 10 (QRM). The spectra show a Compton hump ~ 30 keV which is attributed to the reflection component. The fitting of OBS. 4 returns a $\chi^2_\nu = 1.01$, and OBS. 10 returns $\chi^2_\nu = 1.61$. Then, we fit the spectra with a combined model `constant*tbabs(diskbb+relxillcp)`. Model `relxillcp` is a physical model for relativistic reflection with the `nthcomp` model as the primary source spectrum (García et al. 2014; Dauser et al. 2014). This improves χ^2_ν to 0.92 and 1.00, respectively, thus replacing `powerlaw` by `relxillcp` improves the fitting results. Besides, we tried to fit Obs. 10 with other reflection models `relxilllp` and `relxillpcp`. The `relxilllp` model assumes that the corona is a point source located at a height above the central compact object. Most of the parameters in the `relxilllp`

model are the same as in `relxill`. But instead of the emissivity index, `relxilllp` has two new parameters, h and β , which are the height of the corona and the corona velocity. In the `relxilllpCp` model, the accretion disk is illuminated by a thermal Comptonization spectrum instead of a power-law spectrum in the `relxilllp` model. The fitting returns $\chi^2_\nu = 1.47$ and $\chi^2_\nu = 1.45$.

Usually, if the normalization of LE is fixed to 1, the normalization of ME and HE should be close to 1. There are minor differences between the calibration of the two detectors due to the effects of systematic errors (Li et al. 2020). The relative differences may change slightly during the fitting process. Model `constant` is used for coordinating calibration differences between detectors. In the fitting, we fixed the normalization of LE to 1, the normalizations of ME and HE are set free in the range of 0.85 to 1.15. Model `tbabs` fits

the galactic absorption (Wilms et al. 2000). Due to the uncertain distance of 4U 1630-47, the hydrogen column density remains poorly constrained ($N_H \sim 5\text{--}12 \times 10^{22} \text{ cm}^{-2}$, Yang et al. 2022). Therefore, we set the galactic hydrogen column density N_H free. The reflection model `relxillcp` is used to study the reflection features. We fix the density $\log N = 15$, and the electron temperature in the corona $kT_e = 300 \text{ keV}$ since the fitting is insensitive to their values. The inclination angle of the accretion disk is fixed to 64° , and the spin of BH is fixed to $a = 0.985$. The emissivity for the coronal flavor models q_{in} and q_{out} is linked. The free parameters in the model are the inner radius of the accretion disk (R_{in}), the emissivity index for the coronal flavor models (q_{in} and q_{out}), power-law index of the primary source spectrum (Γ), iron abundance in solar units (A_{Fe}), ionization of the accretion disk ($\log \xi$), reflection fraction parameter (R_f).

The reflection fraction is defined as the ratio of the coronal intensity illuminating the disk to the coronal intensity that reaches the observer, independent of system parameters such as inclination (Dauser et al. 2016). If there is no opaque material blocking the central emission region, the observer will see the sum of the radiation from the primary source and the reflected component. When the source height is reduced, the reflection fraction R_f can increase markedly owing to the light-bending effects near the black hole (Dauser et al. 2016). In addition, the black hole's spin, a , modifies the area of the reflector (the inner edge of the accretion disk) and the amount of reflection. Thus, the reflection fraction can provide valuable insights into the geometry of the reflector (Dauser et al. 2014).

The ionization parameter is defined by:

$$\xi = 4\pi F_X / n_H, \quad (2)$$

where F_X is the flux of irradiation on the accretion disk, n_H is disk hydrogen number density. The value of the ionization parameter ranges from 0 (neutral) to 4.7 (heavily ionized) in the model `relxillcp` and is sensitive to both the disk structure and the coronal illumination (Ballantyne et al. 2011; García et al. 2014). The radial dependence of the irradiation will consequently lead to a radial dependence in terms of ionization as well.

The reflection emissivity is given by:

$$\epsilon(r) = r^{-q}, \quad (3)$$

where q is the emissivity index that can either be constant across all radii or vary with radius. For a point-like X-ray source at height h on the disk axis, the disk irradiation is proportional to $(r^2 + h^2)^{-3/2} \propto r^{-3}$ in the absence of any relativistic effect (Reynolds & Begelman 1997). Therefore, the emissivity profile with index $q = 3$ is considered the standard. However, in the lamp-post geometry, the emissivity profile can vary significantly in the innermost regions depending on the position

of the X-ray source (Wilkins & Fabian 2011; Dauser et al. 2013). Assuming a constant density and ionization across the accretion disk, the emissivity index can reach high values when the source is near the black hole event horizon. Under such conditions, the emissivity profile can be very steep in the inner region of the disk; it flattens and finally reaches $q = 3$ at a further radius (Kammoun et al. 2019).

The best-fitting spectral parameters are listed together in Table 2. The results show that reflection features vary during the outburst. Figure 6 presents the best-fitting spectra and the corresponding data-to-model ratios of observations Num. 4 and 10. Figure 7 shows the relation of centroid frequencies of QPOs and QRM versus reflection fraction, and the centroid frequencies of both QPOs and QRMs are anti-correlated to the reflection fraction with correlation coefficients of -0.97. The evolution of the reflection fraction is presented in the left panel of Figure 8. Comparing two figures (Figures 1 and 8), we find that the reflection fraction has no relation to the fluxes of LE, ME, and HE bands. The hardness ratio positively correlates with the reflection fraction when QPOs are found (with a correlation coefficient of 0.88, see the right panel of Fig. 8). The data in Figures 7 and 8 are fitted with a linear function of $y = \text{slope} \times x + \text{intercept}$, where y is the reflection fraction and x is QPO/QRM frequency or hardness ratio. The lines in the figures represent the best-fitting lines with 90% confidence intervals.

4. DISCUSSION

By comparing the QPOs/QRMs characteristics to the fitted reflection spectral parameters, we find that the QPO centroid frequency anti-correlates to the reflection fraction. The hardness ratio is positively correlated to the reflection fraction when QPOs are detected, and the inner radius of the accretion disk decreases with time when the hardness ratio declines. The decrease in the inner radius of the accretion disk can lead to a variation in the reflection fraction as well as the accretion rate (Dauser et al. 2010, 2014). In addition, the precession of the inner accretion flow can lead to changes in reflection features (Ingram et al. 2009, 2017). Therefore, the correlation between the hardness ratio and QPOs indicates that the QPOs may be generated by precession of the inner flow. The QRM centroid frequency also anti-correlates with the reflection fraction. However, the hardness ratio shows no relation to the reflection fraction when QRM appears. This indicates that QRM has a different physical origin from QPO. Yang et al. (2022) calculated the mHz QRM energy-dependent fractional rms of 4U 1630-47 up to 100 keV. They showed that the mHz QRM phenomenon is more pronounced for non-thermal components, i.e., the corona region. Therefore, the QRM is probably generated from instabilities in the corona. These instabilities can lead to changes in both the corona structure and the reflection properties, and make the QRM centroid

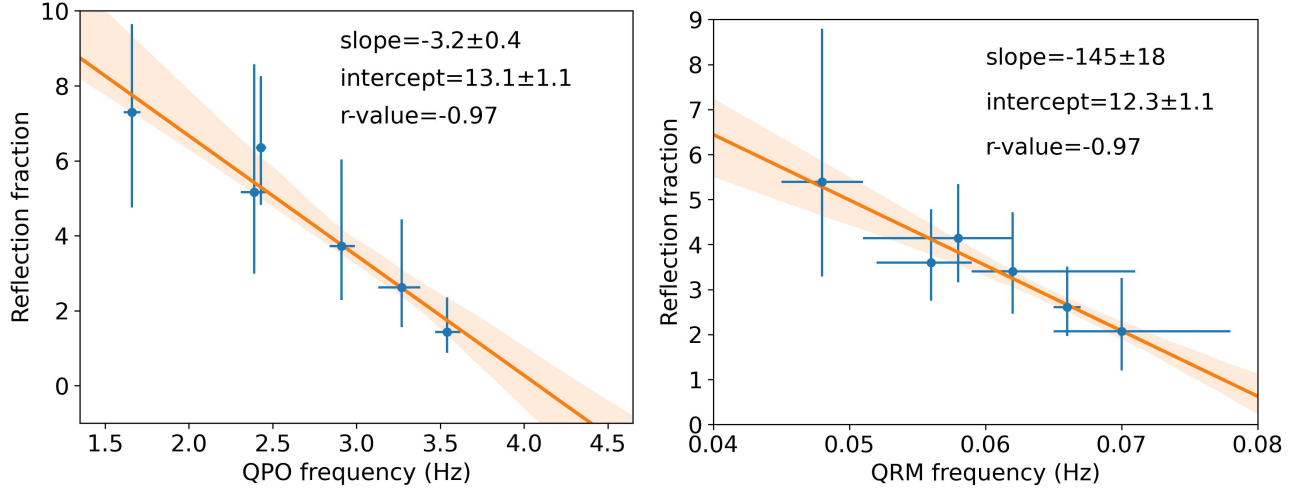


Figure 7. Left: Centroid frequency of QPOs versus reflection fraction and the correlation coefficient between them. **Right:** Centroid frequency of QRMs versus reflection fraction and the correlation coefficient between them. The centroid frequencies of both QPO and QRM are anti-correlated with the reflection fraction. The lines represent the best-fitting lines (90% confidence interval) with a linear function of $y = \text{slope} * x + \text{intercept}$, where y is the reflection fraction and x is the QPO/QRM frequency.

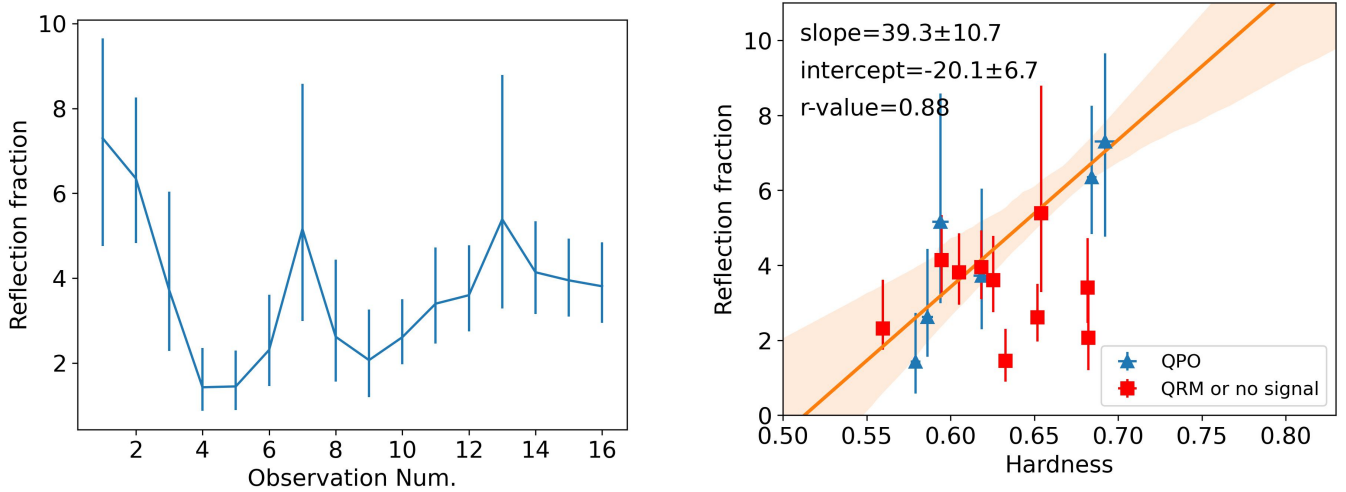


Figure 8. Left: Evolution of reflection fraction versus the observation time during the outburst. The reflection fraction declines in the first 8 observations when QPOs are detected and increases in the later observations when QRMs are detected. **Right:** Hardness ratio (between the LE 2-10 keV and ME 10-35 keV bands) versus reflection fraction for all the observations. Blue triangles are QPO observations, and red squares are QRM observations. The hardness ratio is positively correlated to the reflection fraction when the QPO signal is detected. The hardness ratio shows no relation to the reflection fraction in the case of QRMs or no signals. The line represents the best-fitting line (90% confidence interval) with a linear function of $y = \text{slope} * x + \text{intercept}$, where y is the reflection fraction and x is the hardness ratio.

frequency and reflection fraction related. The appearance of mHz QRMs in 4U 1630-47 is related to the accretion rate, which can be interpreted by the local radiation-dominated disk instability model (Kato et al. 2008). Yang et al. (2022) suggested the mHz QRM could be caused by an unknown accretion instability arising from the corona, leading to flux modulation and variations in the reflection fraction.

To fit the spectra, observations 1-5 require a supersolar iron abundance. So far, no plausible physical explanation has been

proffered for the black-hole systems to be iron-rich. Nonetheless, supersolar prediction for the Fe abundance has been reported in some stellar-mass black hole binaries such as GX 339-4 (García et al. 2015), V404 Cyg (Walton et al. 2017), and Cyg X-1 (Parker et al. 2015). A similar trend is found in AGNs as well, the iron of Seyfert galaxy 1H0707-495 is overabundant by a factor of 10-20 (Fabian et al. 2009; Dauser et al. 2012). García et al. (2018) collected the reports of iron abundance obtained by reflection models for 13 AGNs and 9

BHBs, finding that iron abundance has a trend of a few times over the solar value in both AGNs and BHBs. Observed supersolar iron abundances are unlikely to be realistic, as metal enrichment mechanisms in AGNs and BHBs are expected to be different, and a possible explanation for the results is predicting a relatively low disk density (García et al. 2018). We set the disk density $n_e = 10^{15} \text{cm}^{-3}$ in the fitting. However, the standard α -disk model (Shakura & Sunyaev 1973) and the results of 3D magneto-hydrodynamic (MHD) simulations (Noble et al. 2010; Schnittman et al. 2013) suggest that the accretion disk of black holes has a density orders of magnitude larger than $n_e \sim 10^{15} \text{cm}^{-3}$. Therefore, we set the $\log N$ to 20 (maximum of the model) and re-fit the data of Obs. 1. This still returns a supersolar iron abundance $A_{\text{Fe}} = 2.3^{+3.4}_{-1.4}$, and the disk density may be higher than 10^{20}cm^{-3} . Such a high disk density has been reported in MAXI J1836-194, Dong et al. (2020) reports that it has a high disk density $n_e > 10^{21} \text{cm}^{-3}$. The iron abundance declines to a reasonable range in the later observations, which may be due to the increase in accretion rate and the decrease in the disk density. Since the fitting is insensitive to the value of disk density, the supersolar iron abundance problem could not be resolved with a maximum disk density of the model, we still set the disk density $n_e = 10^{15} \text{cm}^{-3}$ in the fitting.

Our spectral fitting gives a low ionization of about 1.3–1.8 and the ionization gradually increases along with the flux. Ballantyne et al. (2011) used a standard α -disk model (Shakura & Sunyaev 1973) to derive an analytical estimate of $\xi(r)$, their estimation of ξ is nicely independent of the central black hole mass. They also studied how the $\xi(r)$ should depend on various physical parameters such as black hole spin a , coronal dissipation fraction f (Svensson & Zdziarski 1994), and Eddington ratio ($\lambda = L_{\text{bol}}/L_{\text{Edd}}$, where L_{bol} is the bolometric luminosity and L_{Edd} is the Eddington luminosity). The value of ξ is sensitive to Eddington ratio λ , spin a , the radius of peak reflection, and it can be very low at the inner disk for Eddington ratios of a few percent (see Figure 2 in Ballantyne et al. 2011). The Eddington ratio of the source is about 0.03 for Obs. 1 if assuming a black hole mass $M = 10M_{\odot}$ and a distance of 4.7 kpc. Therefore, the low ionization is probably due to the low luminosity of the source and the high disk density.

A steep inner emissivity index (> 8 in most observations) is needed to fit the spectra. Although the emissivity profile with index $q = 3$ is considered as the standard, a steep emissivity index is commonly seen in X-ray binaries and AGNs. This has been reported in X-ray spectral analyses of AGNs, such as MCG-6-30-15 (Fabian et al. 2002; Vaughan & Fabian 2002; Tanaka et al. 2007; Tripathi et al. 2020), 1H0707-495 (Fabian et al. 2009; Zoghbi et al. 2010; Wilkins & Fabian 2011; Dauser et al. 2012), and IRAS 13224-3809 (Ponti et al. 2010), as well as in black hole binaries like XTE J1650-500 (Miniutti et al.

2004), GX 339-4 (Miller 2007), Cyg X-1 (Fabian et al. 2012) and GRS 1915+105 (Tripathi et al. 2020). The observed steep emissivity profiles can be attributed to the following scenarios: (1) a radial profile of the disk ionization or a compact centrally concentrated X-ray corona locates at a low height above the black hole, or the combination of the two (Svoboda et al. 2012; Gonzalez et al. 2017; Liska et al. 2019); (2) a ring-like or disk-like corona locates above the accretion disk with the axis parallel to the black hole (Wilkins & Fabian 2011; Wilkins & Gallo 2013). Additionally, in the compact X-ray source, the radial profile of the disk irradiation shows a significant gradient, resulting in a significant decrease in the ionization parameter as the radius increases (Kammoun et al. 2019). Neglecting this effect can lead to an overestimation of the radial emissivity index if the corona is highly compact and at a low height (Svoboda et al. 2012). The reflection model used in this work assumes the accretion disk has a constant ionization (García et al. 2014; Dauser et al. 2014), which may also be the reason for obtaining a high radial emissivity index in the fitting.

5. CONCLUSION

In this work, we studied the quasi-periodic oscillations and spectral evolutions of 4U 1630-47 during its 2021 outburst based on *Insight*-HXMT observations. Both quasi-periodic oscillations (QPOs) and quasi-regular modulations (QRMs) are detected in the outburst. The QPOs frequencies evolve from $\sim 1.6 - 3.6$ Hz, and QRMs have low frequencies around 0.05 - 0.07 Hz. The reflection components also evolve during the outburst. The QPOs centroid frequency is anti-correlated to the reflection fraction, which is consistent with the prediction of precessing inner flow model (Ingram et al. 2009) and provides evidence for a geometrical origin of QPOs. The centroid frequency of QRMs is also anti-correlated to the reflection fraction. The hardness ratio has a positive correlation with the reflection fraction when QPOs are detected, but shows no relation when the QRMs are detected. This hints that QRMs may have a different physical origin from QPOs. In addition, the mHz QRMs phenomenon is more pronounced for non-thermal emissions above 30 keV. Thus, we suggest that QRMs may be caused by instabilities in the corona.

ACKNOWLEDGEMENTS

We are grateful to the referee for the fruitful comments to improve the manuscript. This work is supported by the National Key Research and Development Program of China (Grants No. 2021YFA0718503 and 2023YFA1607901), the NSFC (12133007). This work has made use of data from the *Insight*-HXMT mission, a project funded by the China National Space Administration (CNSA) and the Chinese Academy of Sciences (CAS).

Table 2. Fitting results of *Insight*-HXMT Observations of 4U 1630-47 in the 2021 outburst with model constant*tbabs(diskbb+relxillcp). The letter P indicates that the error of the parameter was pegged at the upper or lower boundary. All errors were calculated at 90 percent confidence level.

Num.	Tbabs	diskbb			relxillcp					χ^2_ν
	N_H	T_{in}	Norm	R_{in}	q	Γ	$\log \xi$	A_{Fe}	R_f	
	$\times 10^{22} \text{ cm}^{-3}$						erg cm s^{-1}			
1	$6.2^{+0.6}_{-0.7}$	$2.37^{+0.32}_{-0.22}$	$3.2^{+3.0}_{-2.1}$	$-1.14^{+0.12}_{-0.13}$	$6.8^{+2.4}_{-1.4}$	$2.38^{+0.10}_{-0.12}$	$1.3^{+0.6}_{-0.3}$	$3.2^{+3.0}_{-2.1}$	$7.3^{+2.4}_{-2.5}$	1.00
2	$6.5^{+0.3}_{-0.3}$	$2.18^{+0.14}_{-0.12}$	$4.5^{+2.4}_{-1.7}$	$-1.26^{+0.07}_{-0.04}$	$10.0^{+P}_{-2.5}$	$2.40^{+0.06}_{-0.04}$	$1.4^{+0.3}_{-0.3}$	$1.3^{+0.8}_{-0.5}$	$6.4^{+1.9}_{-1.5}$	0.89
3	$6.3^{+0.5}_{-0.7}$	$2.62^{+0.40}_{-0.30}$	$2.7^{+3.1}_{-1.5}$	$-1.00^{+P}_{-0.25}$	$8.3^{+1.5}_{-1.8}$	$2.29^{+0.07}_{-0.08}$	$1.6^{+0.5}_{-0.5}$	$3.3^{+2.9}_{-2.2}$	$3.7^{+2.3}_{-1.4}$	0.99
4	$6.9^{+0.3}_{-0.3}$	$1.88^{+0.30}_{-0.27}$	$5.6^{+5.1}_{-3.8}$	$-1.08^{+0.07}_{-0.10}$	$8.4^{+1.4}_{-1.7}$	$2.32^{+0.06}_{-0.07}$	$1.7^{+1.0}_{-0.6}$	$4.9^{+4.5}_{-3.3}$	$1.4^{+0.9}_{-0.6}$	0.92
5	$7.7^{+0.4}_{-0.5}$	$1.90^{+0.45}_{-0.56}$	$6.8^{+8.6}_{-5.8}$	$-1.12^{+0.10}_{-0.17}$	$8.1^{+1.7}_{-2.4}$	$2.40^{+0.06}_{-0.05}$	$1.7^{+0.8}_{-0.6}$	$1.9^{+3.0}_{-1.3}$	$1.5^{+0.8}_{-0.6}$	1.02
6	$7.0^{+0.4}_{-0.5}$	$2.55^{+0.22}_{-0.19}$	$6.1^{+4.0}_{-2.5}$	$-1.00^{+P}_{-0.24}$	$10.0^{+P}_{-3.9}$	$2.31^{+0.07}_{-0.07}$	$1.6^{+0.5}_{-0.5}$	$0.5^{+1.5}_{-P}$	$2.3^{+1.3}_{-0.9}$	0.92
7	$5.7^{+0.5}_{-0.5}$	$2.60^{+0.35}_{-0.28}$	$3.1^{+2.6}_{-1.6}$	$-1.16^{+0.12}_{-0.10}$	$10.0^{+P}_{-4.0}$	$2.39^{+0.11}_{-0.11}$	$1.6^{+0.4}_{-0.5}$	$0.5^{+2.1}_{-P}$	$5.2^{+3.4}_{-2.2}$	0.97
8	$6.4^{+0.4}_{-0.4}$	$2.11^{+0.31}_{-0.18}$	$5.0^{+4.6}_{-3.1}$	$-1.00^{+P}_{-0.29}$	$6.2^{+3.0}_{-1.8}$	$2.40^{+0.09}_{-0.09}$	$1.5^{+0.4}_{-0.5}$	$0.5^{+1.6}_{-P}$	$2.6^{+1.8}_{-1.1}$	0.94
9	$8.0^{+0.3}_{-0.3}$	$2.58^{+0.22}_{-0.16}$	$8.0^{+3.5}_{-3.0}$	$-1.00^{+P}_{-0.12}$	$10.0^{+P}_{-2.8}$	$2.37^{+0.06}_{-0.06}$	$1.8^{+0.4}_{-0.5}$	$0.5^{+2.8}_{-P}$	$2.1^{+1.2}_{-0.9}$	0.98
10	$8.1^{+0.3}_{-0.3}$	$2.45^{+0.15}_{-0.12}$	$11.1^{+3.9}_{-3.1}$	$-1.00^{+P}_{-0.08}$	$10.0^{+P}_{-2.1}$	$2.47^{+0.04}_{-0.03}$	$1.7^{+0.4}_{-0.4}$	$0.5^{+1.7}_{-P}$	$2.6^{+0.9}_{-0.6}$	1.00
11	$7.7^{+0.3}_{-0.3}$	$2.36^{+0.13}_{-0.11}$	$14.3^{+4.8}_{-3.8}$	$-1.05^{+0.04}_{-0.06}$	$10.0^{+P}_{-2.4}$	$2.39^{+0.05}_{-0.05}$	$1.7^{+0.3}_{-0.5}$	$0.5^{+1.4}_{-P}$	$3.4^{+1.3}_{-0.9}$	1.00
12	$7.7^{+0.3}_{-0.3}$	$2.29^{+0.13}_{-0.12}$	$16.5^{+6.0}_{-5.0}$	$-1.00^{+P}_{-0.07}$	$10.0^{+P}_{-1.7}$	$2.43^{+0.04}_{-0.03}$	$1.7^{+0.3}_{-0.3}$	$0.5^{+1.4}_{-P}$	$3.6^{+1.2}_{-0.9}$	0.94
13	$8.0^{+0.5}_{-0.4}$	$2.30^{+0.25}_{-0.16}$	$14.8^{+8.4}_{-6.7}$	$-1.00^{+P}_{-0.08}$	$10.0^{+P}_{-3.2}$	$2.60^{+0.09}_{-0.07}$	$1.6^{+0.4}_{-0.5}$	$0.5^{+1.4}_{-P}$	$5.4^{+3.4}_{-2.1}$	0.96
14	$7.5^{+0.3}_{-0.2}$	$2.35^{+0.06}_{-0.06}$	$22.6^{+4.0}_{-3.6}$	$-1.00^{+P}_{-0.02}$	$10.0^{+P}_{-1.7}$	$2.44^{+0.04}_{-0.03}$	$1.6^{+0.2}_{-0.3}$	$0.5^{+0.3}_{-P}$	$4.1^{+1.2}_{-1.0}$	0.98
15	$7.8^{+0.2}_{-0.2}$	$2.41^{+0.07}_{-0.05}$	$23.3^{+3.2}_{-3.8}$	$-1.00^{+P}_{-0.02}$	$10.0^{+P}_{-1.5}$	$2.46^{+0.04}_{-0.03}$	$1.7^{+0.2}_{-0.2}$	$0.5^{+0.2}_{-P}$	$4.0^{+1.0}_{-0.9}$	0.95
16	$7.7^{+0.3}_{-0.2}$	$2.39^{+0.06}_{-0.05}$	$26.4^{+3.8}_{-4.2}$	$-1.00^{+P}_{-0.02}$	$10.0^{+P}_{-1.6}$	$2.43^{+0.04}_{-0.03}$	$1.8^{+0.3}_{-0.3}$	$0.5^{+0.3}_{-P}$	$3.8^{+1.0}_{-0.9}$	1.00

REFERENCES

- Altamirano, D., & Strohmayer, T. 2012, *ApJ*, 751, 23
- Altamirano, D., Belloni, T., Linares, M., et al. 2011, *ApJ*, 742, L17
- Arnaud, K. A. 1996, *ASPC*, 101, 17
- Ballantyne, D. R., McDuffie, J. R., & Rusin, J. S. 2011, *ApJ*, 734, 112
- Belloni, T., & Hasinger, G. 1990, *A&A*, 230, 103
- Belloni, T., Homan, J., Casella, P., et al. 2005, *A*, 440, 207
- Belloni, T., Soleri, P., Casella, P., Méndez, M., & Migliari, S. 2006, *MNRAS*, 369, 305
- Belloni, T. M. 2010, Lecture Notes in Physics, Vol. 794, *States and Transitions in Black Hole Binaries* (Springer-Verlag)
- Belloni, T. M., & Motta, S. E. 2016, *ASSL*, 440, 61
- Bu, Q.-c., Chen, L., Li, Z.-s., et al. 2015, *ApJ*, 799, 2
- Cao, X., Jiang, W., Meng, B., et al. 2020, *SCIENCE CHINA Physics, Mechanics & Astronomy*, 63, 1
- Casella, P., Belloni, T., & Stella, L. 2005, *ApJ*, 629, 403
- Chakrabarti, S. K., Debnath, D., Nandi, A., & Pal, P. S. 2008, *A&A*, 489, L41

- Chen, W., Shrader, C. R., & Livio, M. 1997, *ApJ*, 491, 312
- Chen, X., Wang, W., Tang, Y., et al. 2021, *The Astrophysical Journal*, 919, 33
- Chen, Y., Cui, W., Li, W., et al. 2020, *Science China Physics, Mechanics & Astronomy*, 63, 1
- Dauser, T., García, J., Parker, M. L., Fabian, A. C., & Wilms, J. 2014, *MNRAS*, 444, L100
- Dauser, T., García, J., Wilms, J., et al. 2013, *MNRAS*, 430, 1694
- Dauser, T., García, J., Walton, D. J., et al. 2016, *A&A*, 290, A76
- Dauser, T., Wilms, J., Reynolds, C. S., & Brenneman, L. W. 2010, *MNRAS*, 409, 1534
- Dauser, T. s., Svoboda, J. s., Schartel, N. s., et al. 2012, *MNRAS*, 422, 1914
- Dong, Y., García, J. A., Liu, Z., et al. 2020, *MNRAS*, 493, 2178
- Eardley, D. M., Lightman, A. P., & Shapiro, S. L. 1975, *ApJ*, 199, 153
- Fabian, A. C., Rees, M. J., Stella, L., & White, N. E. 1989, *MNRAS*, 238, 729
- Fabian, A. C., Vaughan, S., Nandra, K., et al. 2002, *MNRAS*, 335, L1
- Fabian, A. C., Zoghbi, A., Ross, R. R., et al. 2009, *Natur.*, 459, 540
- Fabian, A. C., Wilkins, D. R., Miller, J. M., et al. 2012, *MNRAS*, 424, 217
- García, J., & Kallman, T. R. 2010, *ApJ*, 719, 695
- García, J., Dauser, T., Lohfink, A., et al. 2014, *ApJ*, 782, 76
- García, J. A., Kallman, T. R., Bautista, M., et al. 2018, *ASPC*, 515, 282
- García, J. A., Steiner, J. F., McClintock, J. E., et al. 2015, *ApJ*, 813, 84
- Gonzalez, A. G., Wilkins, D. R., & Gallo, L. C. 2017, *MNRAS*, 472, 1932
- Grindlay, J. E., Miller, G. F., & Tang, S. 2014, *AAS*, 223, 406.06
- Heil, L. M., Uttley, P., & Klein-Wolt, M. 2015, *MNRAS*, 448, 3348
- Homan, J., Buxton, M., Markoff, S., et al. 2005, *ApJ*, 624, 295
- Homan, J., Klein-Wolt, M., Rossi, S., et al. 2003, *ApJ*, 586, 1262
- Homan, J., Wijnands, R., van der Klis, M., et al. 2001, *ApJS*, 132, 377
- Ichimaru, S. 1977, *ApJ*, 214, 840
- Ingram, A., Done, C., & Fragile, P. C. 2009, *MNRAS*, 397, L101
- Ingram, A., van der Klis, M., Middleton, M., Altamirano, D., & Uttley, P. 2017, *MNRAS*, 464, 2979
- Ingram, A., van der Klis, M., Middleton, M., et al. 2016, *MNRAS*, 461, 1967
- Ingram, A. R., & Motta, S. E. 2019, *New Astron. Rev.*, 85, id. 101524
- Jones, C., Forman, W., Tananbaum, H., & Turner, M. J. L. 1976, *ApJ*, 210, L9
- Kalemci, E., & Maccarone, T. J. and Tomsick, J. A. 2018, *ApJ*, 859, 88
- Kammoun, E. S., Domček, V., Svoboda, J., Dovčiak, M., & Matt, G. 2019, *MNRAS*, 485, 239
- Kato, S. 2001, *PASJ*, 53, 1
- Kato, S., & Fukue, J. 1980, *PASJ*, 32, 377
- Kato, S., Fukue, J., & Mineshige, S. 2008, *Black-Hole Accretion Disks — Towards a New Paradigm —* (Kyoto University Press)
- King, A. L., Walton, D. J., Miller, J. M., et al. 2014, *ApJ*, 784, L2
- Li, X., Li, X., Tan, Y., et al. 2020, *JHEAp*, 27, 64
- Lightman, A. P., & Eardley, D. M. 1974, *ApJ*, 187, L2
- Lightman, A. P., & Rybicki, G. B. 1980, *ApJ*, 236, 928
- Liska, M., Tchekhovskoy, A., Ingram, A., & van der Klis, M. 2019, *MNRAS*, 487, 550
- Liu, C., Zhang, Y., Li, X., et al. 2020, *SCIENCE CHINA Physics, Mechanics & Astronomy*, 63, 1
- Liu, Q., Liu, H., Bambi, C., & Ji, L. 2022, *MNRAS*, 512, 2082
- Miller, J. M. 2007, *ARA&A*, 45, 441
- Miniutti, G., Fabian, A. C., & Miller, J. M. 2004, *MNRAS*, 351, 466
- Miyamoto, S., Kimura, K., Kitamoto, S., Dotani, T., & Ebisawa, K. 1991, *ApJ*, 383, 784
- Molteni, D., Sponholz, H., & Chakrabarti, S. K. 1996, *ApJ*, 457, 805
- Morgan, E. H., Remillard, R. A., & Greiner, J. 1997, *ApJ*, 482, 993
- Motta, S., Homan, J., Muñoz Darias, T., et al. 2012, *MNRAS*, 427, 595
- Motta, S., Muñoz-Darias, T., Casella, P., Belloni, T., & Homan, J. 2011, *MNRAS*, 418, 2292
- Motta, S. E., Casella, P., Henze, M., et al. 2015, *MNRAS*, 447, 2059
- Muñoz-Darias, T., Motta, S., & Belloni, T. M. 2011, *MNRAS*, 410, 679
- Neilsen, J., Remillard, R. A., & Lee, J. C. 2012, *ApJ*, 750, 71
- Noble, S. C., Krolik, J. H., & Hawley, J. F. 2010, *ApJ*, 711, 959
- Novikov, I. D., & Thorne, K. S. 1973, *Black holes (Les astres occlus)*, -, 343
- Parker, M. L., Tomsick, J. A., Miller, J. M., et al. 2015, *ApJ*, 808, 9
- Parmar, A. N., Angelini, L., & White, N. E. 1995, *ApJ*, 452, L129
- Ponti, G., Gallo, L. C., Fabian, A. C., et al. 2010, *MNRAS*, 406, 2591
- Priedhorsky, W. 1986, *Ap&SS*, 126, 89
- Remillard, R. A., & McClintock, J. E. 2006, *ARA&A*, 44, 49
- Remillard, R. A., Morgan, E. H., McClintock, J. E., Bailyn, C. D., & Orosz, J. A. 1999, *ApJ*, 522, 397
- Remillard, R. A., Munro, M. P., McClintock, J. E., & Orosz, J. A. 2002, *ApJ*, 580, 1030
- Reynolds, C. S., & Begelman, M. C. 1997, *ApJ*, 488, 109
- Russell, D. M., Casella, P., Kalemci, E., et al. 2020, *MNRAS*, 495, 182
- Schnittman, J. D., Homan, J., & Miller, J. M. 2006, *ApJ*, 642, 420
- Schnittman, J. D., Krolik, J. H., & Noble, S. C. 2013, *ApJ*, 769, 156

- Seifina, E., Titarchuk, L., & Shaposhnikov, N. 2014, *ApJ*, 789, 57
- Shakura, N. I., & Sunyaev, R. A. 1973, *A&A*, 24, 337
- Sriram, K., Rao, A. R., & Choi, C. S. 2012, *Ā*, 541, 6
- . 2013, *ApJ*, 775, 28
- Stella, L., & Vietri, M. 1998, *ApJ*, 492, L59
- Stella, L., Vietri, M., & Morsink, S. M. 1999, *ApJ*, 524, L63
- Strohmayer, T. E. 2001, *ApJ*, 554, 169
- Sunyaev, R. A., & Truemper, J. 1979, *Nature*, 279, 506
- Svensson, R., & Zdziarski, A. A. 1994, *ApJ*, 436, 599
- Svoboda, J., Dovčiak, M., Goosmann, R. W., et al. 2012, *A&A*, 545, 106
- Syunyaev, R. A., Borozdin, K. N., Aleksandrovich, N. L., et al. 1994, *AstL*, 20, 890
- Tagger, M., & Pellat, R. 1999, *A&A*, 349, 1003
- Tanaka, Y., & Shibazaki, N. 1996, *ARA&A*, 34, 607
- Tanaka, Y., Terashima, Y., Torii, K., et al. 2007, *PASJ*, 59, 315
- Thorne, K. S., & Price, R. H. 1975, *ApJ*, 195, 101
- Tripathi, A., Liu, H., & Bambi, C. 2020, *MNRAS*, 498, 3565
- Trudolyubov, S. P., Borozdin, K. N., & Priedhorsky, W. C. 2001, *MNRAS*, 322, 309
- van den Eijnden, J., Ingram, A., Uttley, P., et al. 2017, *MNRAS*, 464, 2643
- van der Klis, M. 1989, NATO ASI Series, Vol. 262, *Fourier techniques in X-ray timing* (Kluwer Academic / Plenum Publishers)
- Vaughan, S., & Fabian, A. C. 2002, *MNRAS*, 348, 1415
- Wagoner, R. V. 1999, *Phys. Rep.*, 311, 259
- Walton, D. J., Mooley, K., King, A. L., et al. 2017, *ApJ*, 839, 110
- Wang, W., Tang, Y., Tuo, Y., et al. 2021, *Journal of High Energy Astrophysics*, 30, 1
- Weng, S.-S., Wang, T.-T., Cai, J.-P., Yuan, Q.-R., & Gu, W.-M. 2018, *ApJ*, 865, 19
- Wijnands, R., Homan, J., & van der Klis, M. 1999, *ApJ*, 526, 33
- Wilkins, D. R., & Fabian, A. C. 2011, *MNRAS*, 414, 1269
- Wilkins, D. R., & Gallo, L. C. 2013, *MNRAS*, 430, 1694
- Wilms, J., Allen, A., & McCray, R. 2000, *ApJ*, 542, 914
- Yang, Z.-x., Zhang, L., Huang, Y., et al. 2022, *ApJ*, 937, 33
- Zhang, L., Altamirano, D., Uttley, P., et al. 2021, *MNRAS*, 505, 3823
- Zhang, S.-N., Li, T., Lu, F., et al. 2020, *SCPMA*, 63, 249502
- Zhang, W., Jahoda, K., Swank, J. H., Morgan, E. H., & Giles, A. B. 1995, *ApJ*, 449, 930
- Zhu, H., & Wang, W. 2024, *ApJ*, 968, 106
- Zoghbi, A., Fabian, A. C., Uttley, P., et al. 2010, *MNRAS*, 401, 2419